SCIENTIFIC REPORTS

OPEN

SUBJECT AREAS:
NANOPARTICLES
OPTICAL MATERIALS
SENSORS AND BIOSENSORS
NANOPHOTONICS AND PLASMONICS

Received
31 December 2013

Accepted
11 February 2014

Published
27 February 2014

Correspondence and requests for materials should be addressed to M.D.D. (dramican@vinca.rs)

Multifunctional Eu^{3+}- and Er^{3+}/Yb^{3+}-doped $GdVO_4$ nanoparticles synthesized by reverse micelle method

Tamara V. Gavrilović, Dragana J. Jovanović, Vesna Lojpur & Miroslav D. Dramićanin

Vinča Institute of Nuclear Sciences, University of Belgrade, P.O. Box 522, 11001 Belgrade, Serbia.

Synthesis of Eu^{3+}- and Er^{3+}/Yb^{3+}-doped $GdVO_4$ nanoparticles in reverse micelles and their multifunctional luminescence properties are presented. Using cyclohexane, Triton X-100, and *n*-pentanol as the oil, surfactant, and co-surfactant, respectively, crystalline nanoparticles with ~4 nm diameter are prepared at low temperatures. The particle size assessed using transmission electron microscopy is similar to the crystallite size obtained from X-ray diffraction measurements, suggesting that each particle comprises a single crystallite. Eu^{3+}-doped $GdVO_4$ nanoparticles emit red light through downconversion upon UV excitation. Er^{3+}/Yb^{3+}-doped $GdVO_4$ nanoparticles exhibit several functions; apart from the downconversion of UV radiation into visible green light, they act as upconvertors, transforming near-infrared excitation (980 nm) into visible green light. The ratio of green emissions from $^2H_{11/2} \rightarrow {}^2I_{15/2}$ and $^4S_{3/2} \rightarrow {}^4I_{15/2}$ transitions is temperature dependent and can be used for nanoscale temperature sensing with near-infrared excitation. The relative sensor sensitivity is 1.11%K^{-1}, which is among the highest sensitivities recorded for upconversion-luminescence-based thermometers.

The properties of nanoparticles (NPs) and nanostructured materials often drastically differ from those of bulk materials with the same chemical composition and are advantageous for numerous physical, biological, biomedical, and pharmaceutical applications[1]. Therefore, the preparation of nanomaterials with well-controlled shape, size, phase purity, chemical composition, and with targeted, often multifunctional, properties is one of the most challenging problems in materials science. Because multifunctional NPs provide several functionalities in a single assembly, they are more applicable than conventional monofunctional NPs. Consequently, the design and preparation of multifunctional NPs have garnered considerable interest in recent years. In this respect, inorganic NPs doped with small amounts of activator ions such as transition-metal and/or rare-earth (RE) ions have attracted much attention because of their fascinating optical, magnetic, and thermal properties. Their potential as multifunctional materials is exceptionally broad. For example, they can be useful in improving photovoltaic cell efficiency through solar spectral conversion by shifting short-wavelength sunlight (ultraviolet and blue) to longer wavelengths (downshifting, quantum cutting), or by shifting long-wavelength near-infrared (NIR) radiation to visible light (upconversion), which provides more radiation in the spectral region wherein the solar cell shows the largest quantum efficiency[2]. The luminescence decays of the majority of lanthanide and transition-metal ions (of the order of μs and larger) are much longer than those of biological materials (e.g., proteins and cells); therefore, NPs activated with these ions have high potential for biolabeling applications. Long-lasting emissions can be easily discriminated from the autofluorescence of biological materials using time-resolved measurements. Lanthanide- and transition-metal-ion-activated NPs do not show photo-bleaching and blinking, because the emission arises from many ions incorporated within the NPs. Also, these materials can be used in nanomedicine as anticancer drug carriers and magnetic resonance imaging (MRI) contrast agents, as well as in optical displays, cathode ray tubes, fluorescent lamps, light-emitting diodes, infrared detectors, scintillators, and fluorescent paints[3,4].

Gadolinium orthovanadate ($GdVO_4$)-based materials have interesting luminescent and magnetic properties. Gd compounds can be easily doped with luminescent lanthanide ions because of the equal valence and similar ionic radii. They can be efficiently excited with UV radiation because of the strong absorption of the VO_4^{3-} groups and efficient energy transfer from $GdVO_4$ to lanthanide ions. Therefore, $GdVO_4$ is a used as a phosphor (doped with Eu^{3+}, Dy^{3+}, Sm^{3+}), an upconvertor (doped with Er^{3+}/Yb^{3+}, Ho^{3+}/Yb^{3+}, or Tm^{3+}/Yb^{3+}), and a laser (doped with Nd^{3+})[5,6]. In addition, $GdVO_4$ NPs can act as T1-positive contrast agents for MRI, because Gd^{3+} ions possess unpaired electrons that efficiently alter the relaxation time of the surrounding water protons[3,4,7].

So far, several methods have been used to prepare undoped and RE^{3+}-doped $GdVO_4$ NPs with various sizes and shapes. $GdVO_4$:Eu^{3+} NPs have been successfully synthesized via a facile solvothermal route[4,8], a urea hydrolysis method[9], a co-precipitation synthesis[10], as well as facile hydrothermal methods[11,12]. Using these methods, tetragonal particles (d ~ 70 nm), spherical particles (d ~ 40 nm), ellipsoid particles (d ~ 20 nm, l ~ 25 nm), nanorods (d ~ 5 nm, l ~ 20 nm), and nanowires (d = 15 nm, l = a few microns) were fabricated[8–12]. Submicronic polyhedrons with formula $GdVO_4$:RE^{3+} (RE^{3+} = Sm^{3+}, Dy^{3+}, Er^{3+}) (d ~ 300 nm) were obtained by facile hydrothermal methods[13]. Spherical $GdVO^4$:Er^{3+}/Yb^{3+} NPs with diameters ranging from 30 to 50 nm were produced by a simple hydrothermal process assisted by polyvinylpyrrolidone (PVP)[14].

One of the significant methods for the synthesis of nanoparticles with desired diameter and shape is a reverse micelle route. This preparation method is widely applicable and is based on a simple concept. After mixing two reverse micelles, i.e., water-in-oil (oil being the nonpolar organic solvent) droplets containing reaction precursors, an intermicellar exchange readily takes place, and a chemical reaction between the precursors occurs, followed by nucleation and growth of nanocrystals. The growth of the NPs occurs in water droplets dispersed in oil and stabilized by surfactant molecules. In other words, the droplets are coated by monolayer shells of aggregated surfactant molecules, with polar functional fragments (heads) oriented toward the aqueous phase and hydrocarbon chains (tails) immersed in oil. Clearly, the droplet size directly affects the final size of the NPs and depends on the surfactant type and water/surfactant molar ratio. Several other parameters such as the working temperature, concentration of precursor ions, and presence of co-surfactants are important and should be taken into account. The reverse micelle method has already been successfully employed in the preparation of various types of materials, including metals, silica and other oxides, polymers, semiconductors, superconductors, and bimetallic NPs with a core-shell or alloy structure[15–18].

Herein, the aim was to prepare Eu^{3+}- and Er^{3+}/Yb^{3+}-doped $GdVO_4$ NPs by a reverse micelle route and to assess their multifunctional optical properties. The underlying motivation behind this novel synthesis approach to RE vanadates is the expectation that this method can provide small, highly crystalline NPs that incorporate RE dopant ions, and that this approach may be of significance in the preparation of other RE^{3+}-based nanomaterials.

Results and discussion

We synthesized RE^{3+}-doped $GdVO_4$ NPs in a reverse micelle medium using cyclohexane as the oil phase, Triton X-100 as a nonionic surfactant, and n-pentanol as a co-surfactant. In particular, intermediate-chain-length alcohols as co-surfactants (*n*-pentanol, *n*-butanol, or *n*-hexanol) with a hydrophobic chain and a terminal hydroxyl group interact with surfactant monolayers at the interface and get distributed between the aqueous phase and phases in the micellar medium and may affect the final size distribution of the NPs[19,20]. A nonionic surfactant, Triton X-100, was used because of its high degree of flexibility and because it has a much lower critical micelle concentration compared to ionic surfactants owing to the absence of electronic repulsion between ionizable groups[21]. A simplified schematic of our synthesis is shown in Figure 1.

Structural and microstructural properties of Eu^{3+}- and Er^{3+}/Yb^{3+}-doped $GdVO_4$ nanoparticles. Typical X-ray diffraction patterns of Eu^{3+}- and Er^{3+}/Yb^{3+}-doped $GdVO_4$ bulk particles and NPs, together with an example of structural refinement and a schematic representation of a zircon-type structure, are shown in Figure 2. All patterns clearly show the presence of a single tetragonal zircon-type phase of $GdVO_4$ (space group $I4_1/amd$, JCPDS card no. 17-0260)[22]. The absence of impurity phases and very small shift of reflections compared to the reflection positions of pure $GdVO_4$ indicate that the dopant ions are successfully and uniformly incorporated into the $GdVO_4$ host lattice. In addition, the relatively intense reflection peaks suggest that the as-synthesized NPs are highly crystalline, and no additional thermal treatment is necessary. Such a high crystallinity may be attributed to homogeneous nucleation in reverse micelles[23]. The average crystallite sizes of the $GdVO_4$:Eu^{3+} and $GdVO_4$:Er^{3+}/Yb^{3+} NPs (3.3 and 3.9 nm, respectively) are estimated from the diffraction peaks by the Halder–Wagner method, while the value of 4.2 nm is found from structural refinement.

$GdVO_4$ crystallizes with a zircon-type structure (Figure 2c), where the V^{5+} ions in the $[VO_4]^{3-}$ groups are tetrahedrally coordinated with O^{2-} ions, and the Gd^{3+} ions (with D_{2d} point symmetry) are located within a distorted dodecahedron of eight O^{2-} ions. The overall structure is composed of alternating edge-sharing GdO_8 dodecahedra and VO_4 tetrahedra, forming chains parallel to the *c*-axis[24]. The local symmetry (the first coordination sphere) around the lanthanide ions shows the highest effect on their luminescence properties. Consequently, substitution of the Gd^{3+} ions with Eu^{3+} and Er^{3+} will result in emissions that are characteristic of D_{2d} point symmetry.

Structural details of the synthesized Eu^{3+}- and Er^{3+}/Yb^{3+}-doped $GdVO_4$ bulk particles and NPs were calculated by Rietveld refinement using Topas Academic software (Table 1). Rietveld data fit on X-ray diffraction data for $GdVO_4$:Eu^{3+} bulk particles and difference pattern between the simulated and experimental data are shown in Figure 2b. Previous reports on the structure of $GdVO_4$ NPs (see for

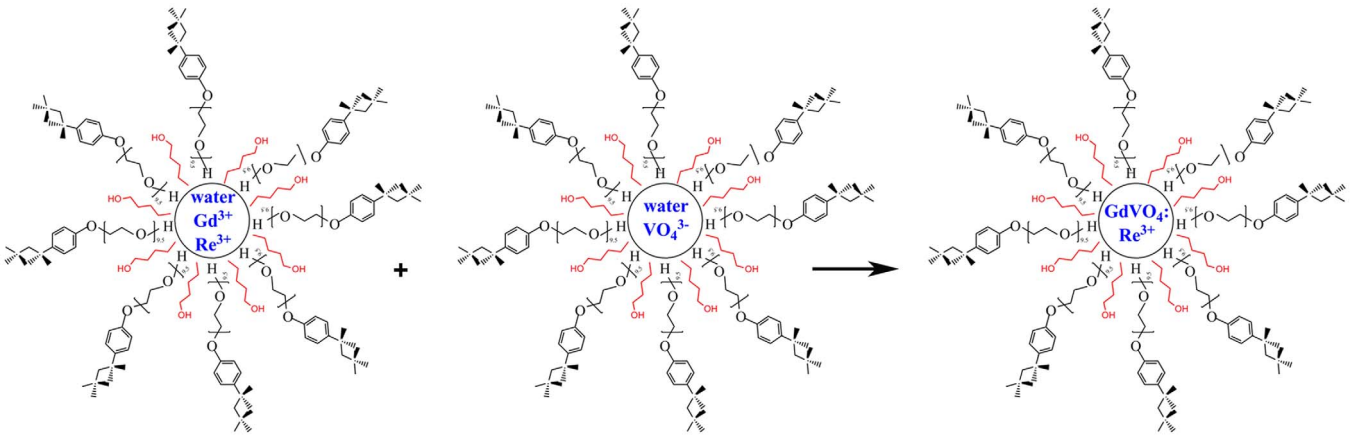

Figure 1 | Simplified schematic of Eu^{3+}- and Er^{3+}/Yb^{3+}-$GdVO_4$ nanoparticle synthesis by reverse micelle method based on Triton X-100/*n*-pentanol/cyclohexane/water system.

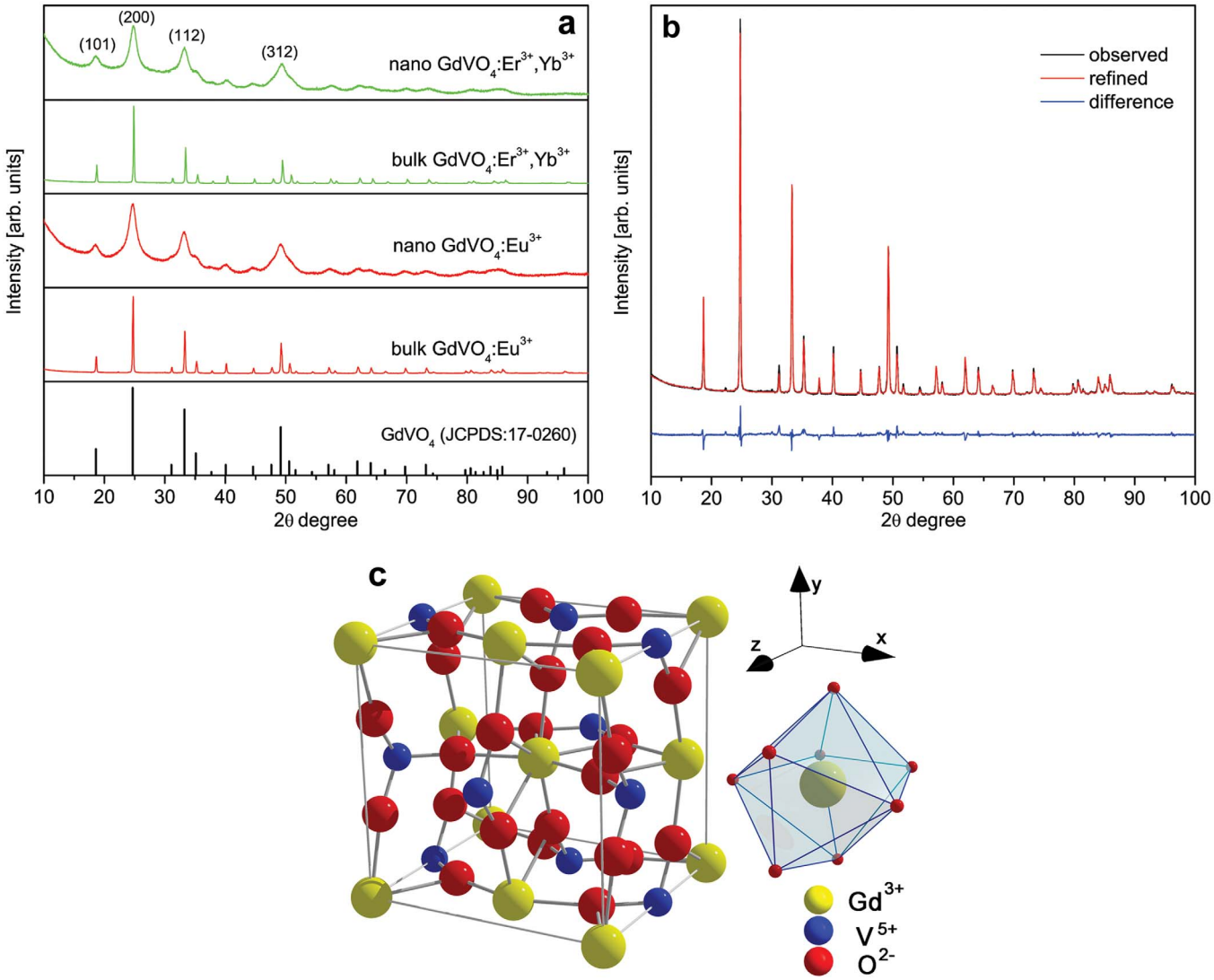

Figure 2 | (a) X-ray diffraction patterns of $GdVO_4$:Eu^{3+} and $GdVO_4$:Er^{3+}/Yb^{3+} bulk particles and nanoparticles, with standard JCPDS data (card No. 17-0260) for tetragonal $GdVO_4$ phase; (b) Rietveld data fit on powder X-ray diffraction data for $GdVO_4$:Eu^{3+} bulk particles and difference pattern between simulated and experimental data; (c) schematic representation of $GdVO_4$ zircon-type crystal structure.

example Refs. 11 and 24) have demonstrated the particle-size-dependent lattice expansion or contraction. In the present study, no significant changes were observed in the lattice parameters between bulk particles and NPs. Particle reduction from micron size to the size of 4 nm induce an increase of 0.42% in cell volumes in the case of Er^{3+}/Yb^{3+}-doped $GdVO_4$ and 0.26% in the case of Eu^{3+}-doped $GdVO_4$. Lattice expansion is related to an increase in the number of surface defects caused by the surface-absorbed molecules, which caused negative surface stress[24].

High-magnification transmission electron microscopy (TEM) images of the $GdVO_4$:Eu^{3+} and $GdVO_4$:Er^{3+}/Yb^{3+} NPs, shown in Figure 3a and 3b, respectively, were measured on nondispersed powders. Lower-magnification TEM images, shown in Figure 3c and 3d, are measured on a grid coated with NPs dispersed in ethanol. The

Table 1 | Structural details of synthesized Eu^{3+}- and Er^{3+}/Yb^{3+}-doped $GdVO_4$ bulk particles and nanoparticles calculated by Rietveld refinement

	bulk $GdVO_4$:Eu^{3+}	nano $GdVO_4$:Eu^{3+}	bulk $GdVO_4$:Er^{3+},Yb^{3+}	nano $GdVO_4$:Er^{3+},Yb^{3+}
Crystallite size (nm)	52(4)	4.19(6)	55(6)	4.30(2)
Strain (%)	0.005	0.0003	0.057	0.0001
R (Bragg)	2.08	0.35	3.59	0.57
$a = b$ (Å)	7.209(7)	7.20(2)	7.174(6)	7.17(2)
c (Å)	6.345(6)	6.37(1)	6.323(5)	6.35(5)
c/a	0.8802	0.8846	0.8814	0.8861
V (Å^3)	329.8(7)	330.6(3)	325.4(6)	326.(2)
Rp (%)	1.44	1.06	2.04	1.41
Rwp (%)	2.27	1.36	3.11	1.95

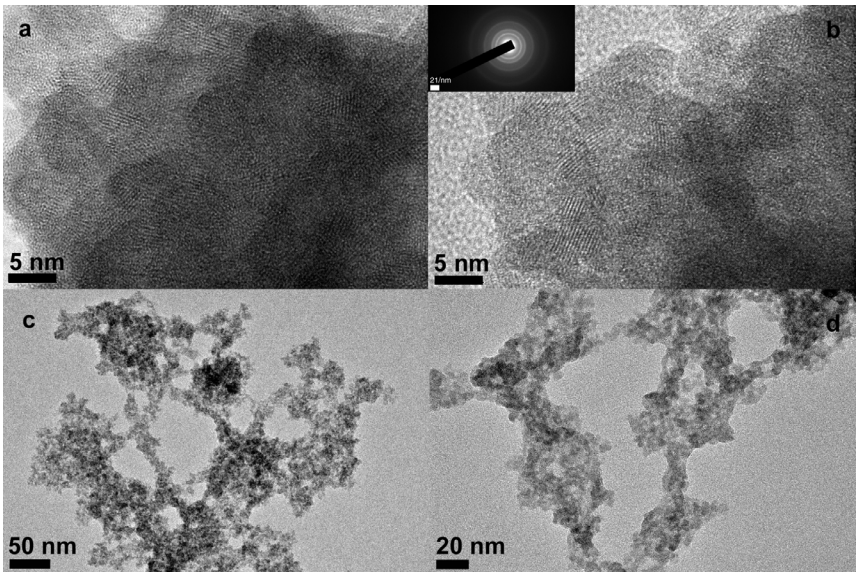

Figure 3 | Transmission electron microscopy images of (a, c) $GdVO_4$:Er^{3+}/Yb^{3+} and (b, d) $GdVO_4$:Eu^{3+} nanoparticles. Images (a) and (b) are obtained on nondispersed powder, and images (c) and (d) are obtained on a grids coated with nanoparticles dispersed in ethanol. Inset shows selected area electron diffraction image of typical $GdVO_4$:Eu^{3+} particle.

TEM images show NPs of ~3–4 nm in diameter. This finding is consistent with the crystallite size evaluated from the powder X-ray diffraction (XRD) measurements. In particular, similar values of the crystalline domain size and microscopically estimated average particle size of the NPs imply that each particle consists of a single crystallite. The selected area electron diffraction (SAED) pattern (inset of Figure 3b) shows features typical to polycrystalline powders with extremely small particles.

Luminescent properties of $GdVO_4$:Eu^{3+}-downshifting photon conversion. Downshifting, or downconversion (DC), is the process of converting high-energy photons into low-energy ones. In RE^{3+}-doped materials, DC usually consists of the absorption of high-energy photons by the host material, energy transfer from the host to the excited states of the RE^{3+} ions, and emission of low-energy photons after radiative relaxation of the excited states of the RE^{3+} ions to the ground state. $GdVO_4$ is an excellent host matrix for downshifting photon conversion. This material shows strong absorption in the UV spectral region and efficient energy transfer to RE^{3+} dopants. The excitation spectra (monitored at 537 nm) of the $GdVO_4$:Eu^{3+} NPs and the bulk material recorded at room temperature are shown in Figure 4a. The spectra share similar features; one can observe broad charge transfer bands (centered at 280 and 320 nm)[25] and several sharp bands at longer wavelengths (350–500 nm) from the absorption by Eu^{3+}.

It is well known that the 320-nm excitation band may be attributed to the VO_4^{3-} groups, i.e., to a V^{5+}–O^{2-} charge transfer (CT) from the excited oxygen ligands (O^{2-}) to the central vanadium atom (V^{5+}) in the VO_4^{3-} ions. According to the molecular orbital theory, this corresponds to transitions from the $^1A_2(^1T_1)$ ground state to the $^1A_1(^1E)$ and $^1E(^1T_2)$ excited states of the VO_4^{3-} ions, i.e., in crystalline $GdVO_4$, the original T_d symmetry of VO_4^{3-} (free ion) is reduced to D_{2d} by the crystal field; this causes a splitting of the degenerate levels of VO_4^{3-}. The 280-nm excitation may be assigned to the combined effects of the V^{5+}–O^{2-} CT and CT transition between Eu^{3+} and O^{2-}. It seems that the V^{5+}–O^{2-} CT occurs much more easily than the CT of Eu^{3+}–O^{2-} because of the large differences in the charge and ionic radii between V^{5+} (+5, r = 0.0355 nm) and Eu^{3+} (+3, r = 0.107 nm)[22,26–28]. The excitation spectra above 350 nm exhibit sharp lines at 363, 377, 381, 395, 418, and 466 nm, which exclusively correspond to the following *f*–*f* transitions within the $4f^6$ electronic shell of Eu^{3+} ions: $^7F_0 \rightarrow {}^5D_4$, $^7F_0 \rightarrow {}^5G_4$, $^7F_0 \rightarrow {}^5G_2$, $^7F_0 \rightarrow {}^5L_6$, $^7F_1 \rightarrow {}^5L_6$, and $^7F_0 \rightarrow {}^5D_2$, respectively. The absorption of VO_4^{3-} is stronger than that of Eu^{3+}, because the *f*–*f* electronic transitions of lanthanides are spin-forbidden. However, Figure 4a shows that this difference is much more pronounced in the NPs than in the bulk particles.

The room-temperature DC emission spectra of $GdVO_4$:Eu^{3+} NPs and the bulk material, recorded under excitation at 330 nm, are shown in Figure 4b. For the sake of convenience, the emission intensity values of the bulk material (because they are much larger) are scaled down by a factor of 100. As is known, the emission intensities of RE^{3+}-doped materials are generally lower for nanocrystals; this phenomenon can be explained by surface effects. Nano-sized particles possess a higher surface-area-to-volume ratio and many ligating species on their surface; therefore, a larger portion of RE^{3+} emissions is quenched.

The emission spectra are dominated (in the range above 500 nm) by the red $^5D_0 \rightarrow {}^7F_2$ electronic transition of Eu^{3+} at 618 nm, while three weaker lines at 537, 551, and 593 nm can be attributed to the $^5D_1 \rightarrow {}^7F_1$, $^5D_1 \rightarrow {}^7F_2$, and $^5D_0 \rightarrow {}^7F_1$ transitions, respectively. Further, the spectrum of the NPs shows an intense, broad band with a maximum at ~400 nm attributed to the vanadate group emission. However, the emissions from the vanadate groups are much smaller than those from Eu^{3+} in the bulk material, which further confirms the more pronounced nonradiative relaxation (quenching) of Eu^{3+} in the NPs than that in the bulk material. Nevertheless, emission from the $GdVO_4$:Eu^{3+} NPs is sufficiently strong to be easily recorded. A schematic representation of the transitions responsible for the emission spectrum is shown in Figure 4c.

It is well known that the emission of Eu^{3+} ions can serve as a sensitive probe of local site symmetry[29,30]. It is possible to deduce the local symmetry around the Eu^{3+} ion from the number of multiplet–multiplet transition bands. Moreover, the relative intensities of the transitions also provide some information about the local symmetry. When Eu^{3+} occupies a site with an inversion center, the magnetic-dipole transition of $^5D_0 \rightarrow {}^7F_1$ (orange) is dominant. On the contrary, the electric-dipole transition of $^5D_0 \rightarrow {}^7F_2$ (red) will be dominant when Eu^{3+} occupies a site without an inversion center. Here, the shape of the emission spectra (Figure 4b) confirms that the Eu^{3+} ions occupy sites with D_{2d} point symmetry (sites without an inversion center), i.e., they replace the Gd^{3+} ions. This finding further confirms and complements those from the XRD results[31,32].

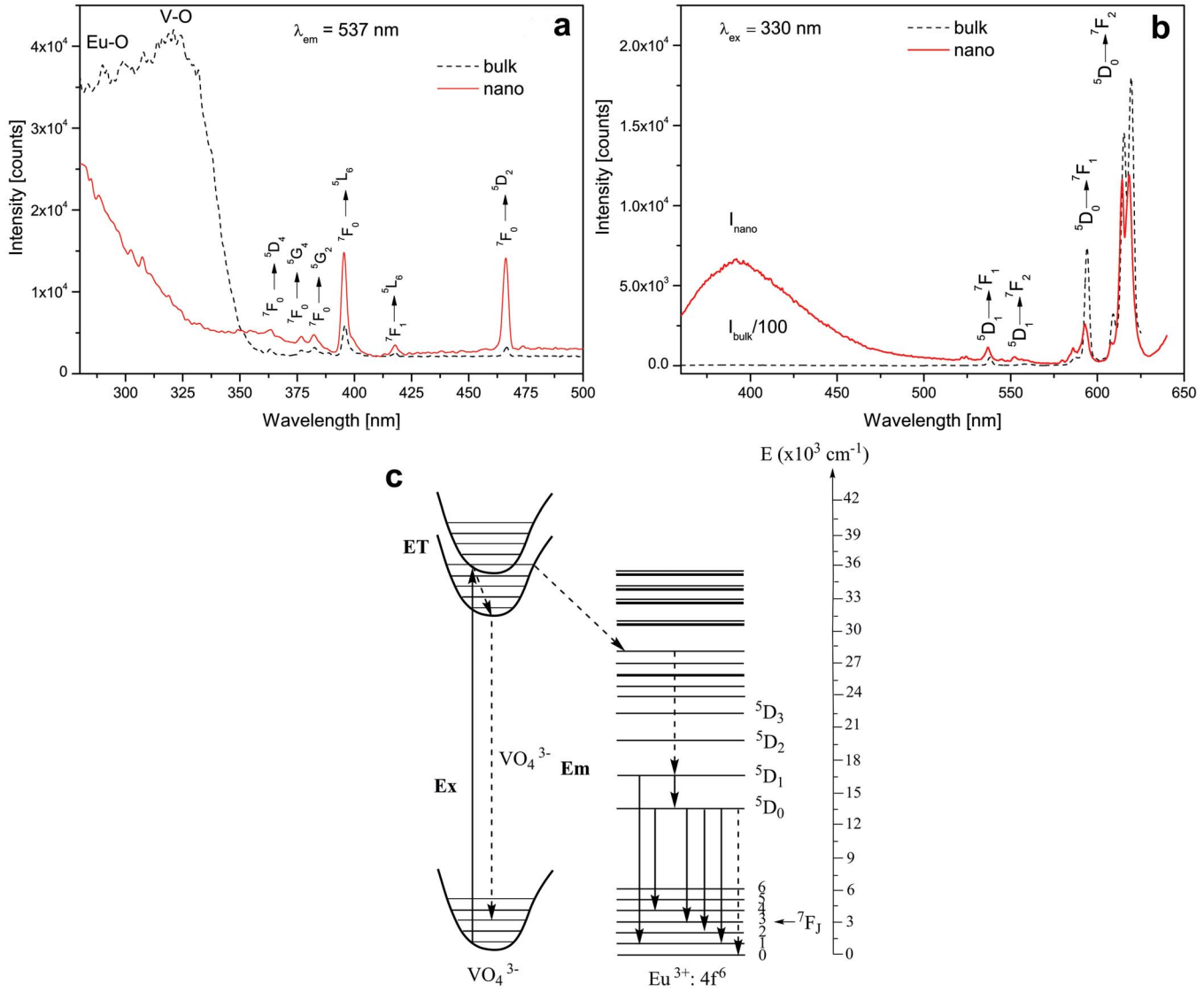

Figure 4 | (a) Room-temperature excitation spectra and (b) downconversion (DC) emission spectra of bulk and nano-sized $GdVO_4$:6mol%Eu^{3+}. (c) Energy levels and transitions in Eu^{3+}.

Apart from the smaller emission intensities in the NPs compared to the bulk material, no other differences between the emission spectra could be observed (no changes in the band shapes and no band shifts). By taking into account the high sensitivity of Eu^{3+} luminescence to changes in the symmetry of the local environment, it was found that negligible lattice aberrance in nanoparticles is confirmed by the absence of modulation of emission. Therefore, it is reasonable to conclude that reduction in the particle size does not produce any considerable changes in the crystal structure of $GdVO_4$ particles.

In solid materials, electrons in the $4f^n$ orbitals of lanthanides are highly localized; therefore, such electrons do not exhibit quantum confinement even in nanocrystals[33]. Nanophenomena due to size confinement in lanthanide nanoparticles may occur through changes of ion–phonon coupling, which influence the dynamics of 4f–4f transitions, whereas the static energy levels of the 4f states experience negligible impact. In fact, majority of reported size-reduction effects on lanthanide luminescence from 4f-4f transitions are not results of nano-confinement on electronic states. They are the consequences of induced structure distortion and surface defects that affect the local environments (site symmetry) surrounding the lanthanide ions. In contrast to lanthanide $4f^n$ states, the electronic states of VO_4^{3-} ions are sensitive to the particle size. This is also the case with the lanthanide $4f^{n-1}5d$ states, which, however, are not of relevance for the current study. In these cases, electronic transitions between states are spin-allowed, whereas the transitions between $4f^n$ states are spin-forbidden. Therefore, the size effect appears in VO_4^{3-} transitions and is responsible for the difference in the excitation spectra shown in Figure 4a.

Luminescent properties of GdVO4:Er^{3+}/Yb^{3+}: upconversion and downconversion. In upconversion (UC), the sequential absorption of two or more photons (via intermediate long-lived energy states) leads to the emission of light at a shorter wavelength than the excitation wavelength. The most important class of UC materials are based on transparent inorganic insulators doped with RE^{3+} ions, because these ions have many long-lived energy states. UC NPs are of particular interest because of the following reasons: they have huge potential in biomedical applications (excitation in the NIR spectral region where biological materials have minimal absorption); they can be used to improve the solar cell efficiency (because NP layers scatter considerably less light than bulk particles); and it is possible to fine-tune the various properties of NPs for a specific purpose by controlling their shape and size at the nanometer scale[34].

Figure 5a and 5b presents the room-temperature UC emission spectra of the $GdVO_4$:Er^{3+}/Yb^{3+} NPs and the bulk material and a schematic illustration of the energy levels and transitions for the Yb^{3+}/Er^{3+} system, respectively. Their emission spectra were measured upon excitation with 980-nm radiation under identical conditions for comparing the emission intensities.

Er^{3+}/Yb^{3+} doping of materials, where Yb^{3+} is used as a sensitizing ion and Er^{3+} is used for providing the emission, is by far the most frequently used method for preparing RE-based UC materials. This is because Yb^{3+} shows good absorption in the NIR spectral region (~980 nm) and a simple energy-level structure with only two levels whose energy difference closely matches that of Er^{3+}; also, energy transfer from Yb^{3+} to Er^{3+} is efficient. The observed UC emission peaks (Figure 5a) are characteristic of Er^{3+} emission and are present in both the green ($^2H_{11/2} \rightarrow {}^4I_{15/2}$ and $^4S_{3/2} \rightarrow {}^4I_{15/2}$ transitions) and red ($^4F_{9/2} \rightarrow {}^4I_{15/2}$ transition) spectral regions.

A schematic representation of the processes responsible for UC emission is shown in Figure 5b. The energy of the $^4I_{11/2}$ level of Er^{3+} is very similar to that of the $^2F_{5/2}$ level of Yb^{3+}; thus, both Er^{3+} and Yb^{3+} absorb 980-nm photons. However, the absorption cross section of the $^2F_{7/2} \rightarrow {}^2F_{5/2}$ transition of Yb^{3+} is very large than that of the $^4I_{15/2} \rightarrow {}^4I_{11/2}$ transition of Er^{3+}; therefore, the Yb^{3+} ions absorb most of the excitation energy. The excited Yb^{3+} ions either relax to the ground state ($^2F_{7/2}$) or participate in energy transfer to the neighboring Er^{3+} ions. Therefore, the energy levels of Er^{3+} are populated by ground- and excited-state absorption and by the charge transfer from the Yb^{3+} ions. Because of the long-lasting nature of the Er^{3+} excited states, its higher energy levels can be populated after the absorption of two or more photons by a combination of the above-mentioned processes. The radiative relaxation of these higher energy states produces UC emission. In the cases of relaxation from $^2H_{11/2}$ and $^4S_{3/2}$ (green emission) and $^4F_{9/2}$ (red emission) to the Er^{3+} ground state ($^4I_{15/2}$), the overall UC process requires the absorption of two photons in each case. UC emission from the NPs is less intense than the emission from the bulk material for the same reasons as for the DC emission with Eu^{3+}. Also, in this case, no changes in the band shapes between the NP and bulk emission are observed, and the same ratio of green to red emission is present.

The room-temperature DC emission spectra of the $GdVO_4$:Er^{3+}/Yb^{3+} NPs and the bulk material recorded under excitation at 345 nm are shown in Figure 6. Two green bands are observed at ~525 and ~555 nm, which correspond to the transitions from the excited-state levels $^2H_{11/2}$ and $^4S_{3/2}$ to the Er^{3+} ground state ($^4I_{15/2}$). Note that very weak red emission (~625 nm) corresponding to the $^4F_{9/2} \rightarrow {}^4I_{15/2}$ transition is also observed, in contrast to the UC spectra upon 980-nm excitation (Figure 5b). This demonstrates that the $^4F_{9/2}$ state responsible for the red emission is not populated via the $^4F_{7/2}$ and $^4S_{3/2}$ levels or the upper levels, but by lower-lying levels via re-excitation[35].

Temperature dependence of upconversion emission in Er^{3+}/Yb^{3+}-doped $GdVO_4$ nanoparticles. Luminescence thermometry is a promising approach for temperature sensing in a nanoscale environment[36–38]. Temperature evolution can be realized by remotely measuring the changes in the luminescent properties of the various types of NPs or organic dyes. This approach provides temperature measurements with spatial resolution of less than 1 μm, which cannot be achieved with traditional thermometers, and can be highly beneficial in biomedicine, micro/nano-electronics, and integrated photonics[37]. Temperature sensing with upconverting NPs is of particular interest for biomedicine, because the excitation typically occurs in the NIR spectral region, and therefore, autofluorescence (the natural emission of light by biological structures such as mitochondria and lysosomes when they absorb light) from biological material does not affect the measurements. NIR excitation shows excellent tissue penetration, and a large number of rather inexpensive light sources operating in this spectral region exist. Here, the potential of the Er^{3+}/Yb^{3+}-doped $GdVO_4$ NPs for temperature sensing is assessed. The UC emission spectra of the $GdVO_4$:Er^{3+}/Yb^{3+} NPs recorded over the temperature range 307–473 K are shown in Figure 7.

Because two closely separated levels show Boltzmann-type relative population, the integrated fluorescence intensity ratio (FIR) of transitions from the $^2H_{11/2}$ and $^4S_{3/2}$ levels to the ground level could be approximated using Boltzmann distribution as follows[39]:

$$FIR = \frac{I\left(^2H_{11/2} \rightarrow {}^4I_{15/2}\right)}{I\left(^4S_{3/2} \rightarrow {}^4I_{15/2}\right)} = \frac{g_H A_H h\nu_H}{g_S A_S h\nu_S} \exp\left(-\frac{\Delta E}{kT}\right) = B \exp\left(-\frac{\Delta E}{kT}\right) \quad (1)$$

where g_H and g_S are the degeneracies of the $^2H_{11/2}$ and $^4S_{3/2}$ levels, respectively; A_H, A_S and ν_H, ν_S are the spontaneous emission rates and frequencies of the $^2H_{11/2} \rightarrow {}^4I_{15/2}$ and $^4S_{3/2} \rightarrow {}^4I_{15/2}$ transitions, respectively; h is the Planck's constant; k is the Boltzmann's constant; and T is the absolute temperature. Equation (1) can be expressed as follows:

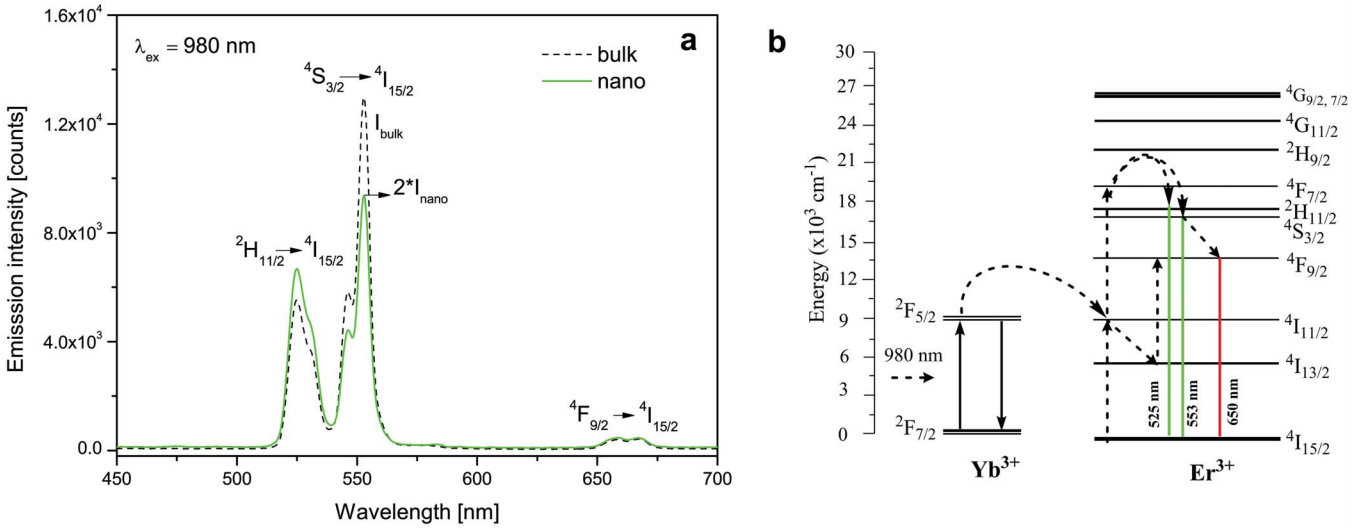

Figure 5 | (a) Room-temperature upconversion (UC) emission spectra of $GdVO_4$: 2mol%Er^{3+}, 10mol%Yb^{3+} nanoparticles and bulk material. (b) Partial energy-level diagrams of Er^{3+} and Yb^{3+} with proposed upconversion mechanism.

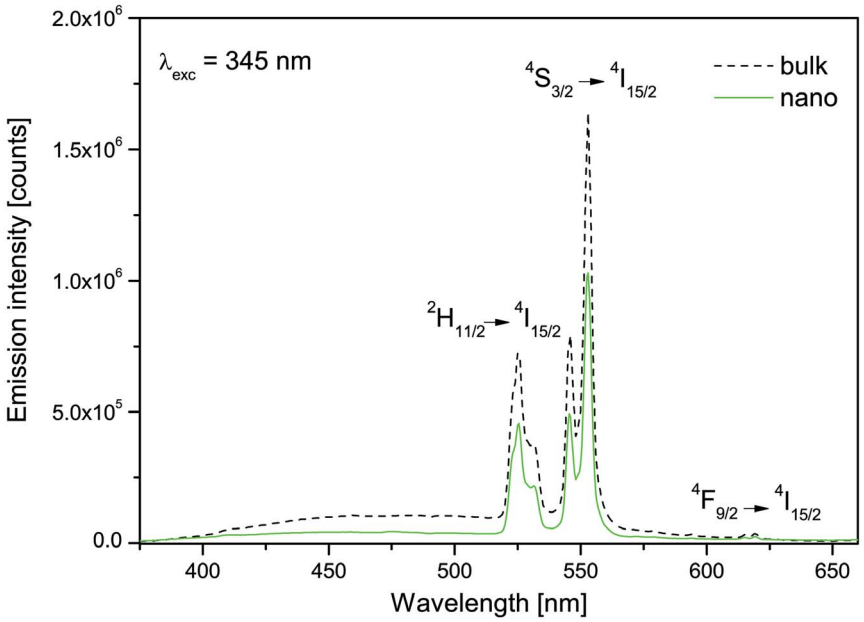

Figure 6 | Room-temperature downconversion (DC) emission spectra of $GdVO_4$:2mol%Er^{3+}, 10 mol%Yb^{3+} nanoparticles and bulk material.

$$\ln(FIR) = \ln(B) + \left(-\frac{\Delta E}{kT}\right) = \ln(B) + \left(-\frac{C}{T}\right), \qquad (2)$$

where B and C are the constants that need to be determined.

Fitting of the experimental data with Equation (2), shown in Figure 8a, shows good correlation between experiment and theory, and is also in agreement with previous reports on thermometry performed using Er^{3+} UC emission[38,39]. The obtained parameters, $\log(B) = 2.81$ and $C = 1047.52\ cm^{-1}$, provide the absolute sensor sensitivity, S_a [in K^{-1}]:

$$S_a = \left|\frac{\partial FIR}{\partial T}\right| = FIR \times \frac{\Delta E}{kT^2}, \qquad (3)$$

and the relative sensor sensitivity, Sr [in $\%K^{-1}$]:

$$S_r = 100\% \times \left|\frac{1}{FIR}\frac{\partial FIR}{\partial T}\right| = 100\% \times \frac{\Delta E}{kT^2}. \qquad (4)$$

The sensitivity values calculated from Equations (3) and (4) are shown in Figure 8b. The maximal value of the relative sensitivity, $1.11\%K^{-1}$, is found at 307 K; it is very similar to those found in $NaYF_4$:Yb^{3+},Er^{3+}[40,41] and gold-decorated Gd_2O_3:Yb^{3+},Er^{3+}[39]. This result is among the highest relative sensitivities of thermometers based on UC emission (for a comparison see Table S1 in the Supporting Information of Ref. 38). A temperature resolution of ~1 K can be estimated from $\delta FIR/S_a$, where δFIR is the resolution of the FIR calculated from the standard deviation of the residuals in the polynomial interpolation of the experimental data points (temperature vs. FIR curve)[36,39]. Information on the temperature resolution may also be deduced from the sensitivity of the detection system and the calculated sensitivity.

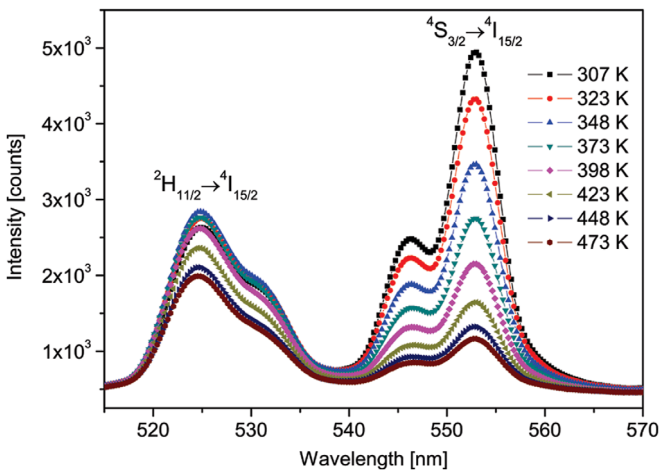

Figure 7 | Upconversion emission spectra of $GdVO_4$:Er^{3+}/Yb^{3+} nanoparticles recorded over the temperature range 307–473 K.

In conclusion, preparation of $GdVO_4$ powders using reverse micelles yields super thin NPs (3–4 nm in diameter) because of homogeneous nucleation. A zircon-type structure that incorporates Eu^{3+} or Er^{3+}/Yb^{3+} ions as dopants can be achieved without additional thermal treatments; therefore, no further growth of the particles occurs. Moreover, in the absence of thermal treatment and because the particles were conserved in micelles, each particle consists of a single crystallite, as evidenced from the crystal coherence size obtained from the XRD analysis and the particle size from the TEM images. Different optical functions are observed with Eu^{3+} and Er^{3+}/Yb^{3+} doping. In DC, the Eu^{3+}-doped $GdVO_4$ NPs exhibit characteristic sharp emissions in the red region along with broad emissions from the vanadate groups centered at 400 nm. The intensity of the Eu^{3+} emission is much smaller in the NPs than in the bulk powders. This indicates that stronger nonradiative pathways exist in the NPs because of the presence of ligands on their surface. No changes in the band positions or bandwidths are observed in the emission spectra of the NPs and bulk particles; this result suggests that were no significant alterations of the size and symmetry of the first coordination sphere around the dopant ions upon decreasing the particle size to the nanoscale. The Er^{3+}/Yb^{3+}-doped NPs emit green light with both DC and UC processes. Similar to the Eu^{3+} luminescence, NPs show smaller emissions compared to the bulk particles, and no changes in the band shapes or positions are observed. However, these emissions are of sufficient strength to be easily detected and used; for example, in temperature sensing by UC emission. This might be a new and powerful function of Er^{3+}/Yb^{3+}-doped $GdVO_4$ NPs; luminescence nanoprobes can be used to extract information about the local temperature of a given system with submicrometric spatial resolution, which cannot be achieved with

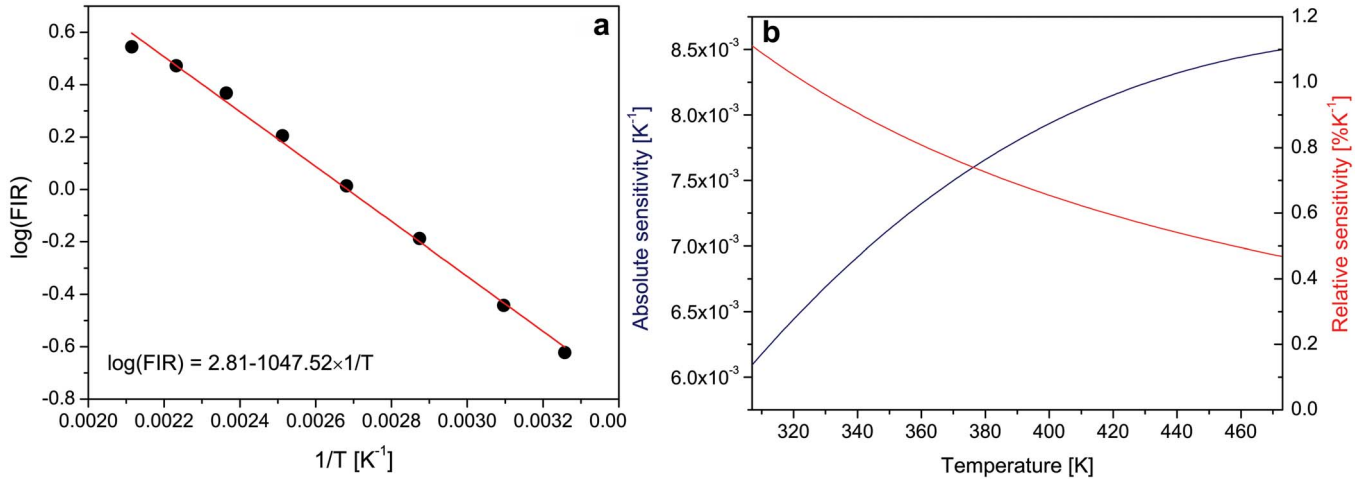

Figure 8 | (a) Fluorescence intensity ratio (FIR) values of $GdVO_4$:Er^{3+}/Yb^{3+} nanopowder as a function of temperature (dots) and corresponding line obtained by fitting Equation (2). (b) Absolute (blue line) and relative (red) sensitivity of FIR temperature sensor based on the upconversion of $GdVO_4$:Er^{3+}/Yb^{3+} nanopowder.

traditional temperature sensors. Compared to other materials recently suggested for use in temperature sensing with UC, Er^{3+}/Yb^{3+}-doped $GdVO_4$ NPs exhibit a high relative sensitivity (of 1.11%K^{-1}) with an estimated resolution of 1 K.

Furthermore, temperature sensing with UC emission utilizes excitation sources in the NIR spectral region, where biological tissues show low absorption; therefore, this type of sensor may have valuable applications in the biomedicine and bioimaging fields. $GdVO_4$ can act as a T_1-positive contrast agent, because Gd^{3+} ions possess unpaired electrons that could efficiently alter the relaxation time of the surrounding water protons. Phosphorescent emission of RE^{3+}-doped materials is useful for bioimaging, because it lasts longer than the autofluorescence of tissue, and thus, can be easily discriminated using time-resolved measurements. Also, unlike semiconducting quantum dots, RE^{3+}-doped NPs do not show photobleaching. Therefore, these NPs, because of their exceptionally small sizes, excellent crystallinity, and phosphorescent emission with the possibility to sense temperature with a high spatial resolution, show significant potential for bioimaging and biolabeling.

Methods

Synthesis of Eu^{3+}- and Er^{3+}/Yb^{3+}-doped $GdVO_4$ nanoparticles by reverse micelle method. The following chemicals were used as received: gadolinium(III) nitrate hexahydrate, $Gd(NO_3)_3{\cdot}6H_2O$ (99.9%, Alfa Aesar), europium(III) nitrate hexahydrate, $Eu(NO_3)_3{\cdot}6H_2O$ (99.9%, Alfa Aesar), erbium(III) nitrate pentahydrate, $Er(NO_3)_3{\cdot}5H_2O$ (99.9%, Alfa Aesar), ytterbium(III) nitrate pentahydrate, $Yb(NO_3)_3{\cdot}5H_2O$ (99.9%, Alfa Aesar), ammonium vanadium oxide, NH_4VO_3 (min. 99.0%, Alfa Aesar), and sodium hydroxide, NaOH (min. 99%, Moss Hemos).

A typical high-temperature solid-state reaction method was used for preparing RE^{3+}-doped $GdVO_4$ bulk material; more details can be found in our previous work[22]. The $GdVO_4$:Eu^{3+} and $GdVO_4$:Er^{3+}/Yb^{3+} NPs were prepared by a reverse micelle method. The doping levels were 6 mol% of Eu^{3+} and 2 mol% of Er^{3+}/10 mol% of Yb^{3+}.

A typical synthesis using reverse micelles at room temperature was as follows. First, the following solutions were prepared: 1) an oil phase formed by mixing cyclohexane (100 mL), Triton X-100 (60 mL), and *n*-pentanol (20 mL) in a volume ratio of 5 : 3 : 1; 2 a) a solution (10 mL) formed by mixing aqueous solutions of 0.1 M $Gd(NO_3)_3{\cdot}6H_2O$ and 0.1 M $Eu(NO_3)_3{\cdot}6H_2O$ in a stoichiometric ratio (6 mol% Eu^{3+} with respect to Gd^{3+}); 2 b) a solution (10 mL) formed by mixing aqueous solutions of 0.1 M $Gd(NO_3)_3{\cdot}6H_2O$ (10 mL) and 0.1 M $Er(NO_3)_3{\cdot}6H_2O$ and 0.1 M $Yb(NO_3)_3{\cdot}6H_2O$ in a stoichiometric ratio (2 mol% Er^{3+} and 10 mol% Yb^{3+} with respect to Gd^{3+}); and 3) a 0.1 M solution of Na_3VO_4 (10 mL) formed by dissolving NH_4VO_3 in 0.15 M NaOH. In the next step, the oil phase and solution containing VO_4^{3-} were mixed; into the obtained mixture, the solution containing RE^{3+} was added drop-wise under continuous magnetic stirring. In all syntheses, the water-to-oil volume ratio was maintained at 1 : 9.

At the end of each synthesis, a stable (single-phase) yellowish colloid solution containing reverse micelles was obtained upon stirring for 60 min at room temperature. After aging for 24 h, methanol was added to destabilize the solution. The obtained mixture was separated by centrifugation, and the resulting precipitate (powder) was washed several times with methanol and water to remove excess surfactant and then dried in an oven at 70°C for 20 h.

Characterization. XRD measurements were performed on a Rigaku SmartLab diffractometer using Cu-K_α radiation (λ = 0.15405 nm). Diffraction data were recorded with a step size of 0.02° and a counting time of 0.7° min^{-1} over the angular range 10° ≤ 2θ ≤ 100°. Crystallite sizes were estimated using the Halder–Wagner method by analyzing all major diffraction peaks. TEM imaging was performed using a JEOL-JEM 2100 instrument (Akishima-shi, Japan) equipped with a LaB_6 cathode operating at 200 kV.

Photoluminescence measurements were carried out on pellets prepared from RE^{3+}-$GdVO_4$ powders under a load of 2 ton cm^{-2}. All DC luminescence measurements were performed at room temperature using a Fluorolog-3 spectrofluorometer (model FL3-221, Horiba Jobin Yvon), which uses a 450-W xenon lamp as an excitation source for emission measurements (λ_{exc} = 330 nm for $GdVO_4$:Eu^{3+} and λ_{exc} = 345 nm for $GdVO_4$:Er^{3+}/Yb^{3+}) and a xenon–mercury pulsed lamp for decay time measurements. The emission spectra were scanned in the wavelength ranges 350–640 and 375–660 nm, respectively. The UC emission spectra were measured upon excitation with 980-nm radiation (MDLH 980 3w) on an AvaSpec-2048 Fiber Optic Spectrometer system.

1. Albanese, A., Tang, P. S. & Chan, W. C. The effect of nanoparticle size, shape, and surface chemistry on biological systems. *Annu. Rev. Biomed. Eng.* **14**, 1–16 (2012).
2. Huang, X., Han, S., Huang, W. & Liu, X. Enhancing solar cell effciency: the search for luminescent materials as spectral converters. *Chem. Soc. Rev.* **42**, 173–201 (2013).
3. Yen, W. M., Shionoya, S. & Yamamoto, H. *Phosphor Handbook* (CRC Press, Boca Raton, FL, USA, 2007).
4. Nuñez, N. O. *et al.* Surface modified Eu:$GdVO_4$ nanocrystals for optical and MRI imaging. *Dalton Trans.* **42**, 10725–10734 (2013).
5. Singh, N. S. *et al.* Re-dispersion and film formation of $GdVO_4$:Ln^{3+} (Ln^{3+} = Dy^{3+}, Eu^{3+}, Sm^{3+}, Tm^{3+}) nanoparticles: particle size and luminescence studies. *Dalton Trans.* **41**, 4404–4412 (2012).
6. Zhang, L. *et al.* Characteristics of Nd:$GdVO_4$ laser with different Nd-doping concentrations. *Chin. Phys. Lett.* **23**, 2088–2091 (2006).
7. Kang, X. *et al.* Poly(acrylic acid) modified lanthanide-doped $GdVO_4$ hollow spheres for up-conversion cell imaging, MRI and pH-dependent drug release. *Nanoscale* **5**, 253–261 (2013).
8. Kim, M.-J. & Huh, Y.-D. Preparation and photoluminescence of GdVO4:Eu nanophosphors for flexible and transparent displays. *Bull. Korean Chem. Soc.* **32**, 4454–4457 (2011).
9. Singh, N. S. *et al.* Luminescence study of Eu^{3+} doped $GdVO_4$ nanoparticles: Concentration, particle size, and core/shell effects. *J. Appl. Phys.* **104**, 104307 (9pp) (2008).
10. Jovanović, D. J. *et al.* Annealing effects on the microstructure and photoluminescence of Eu^{3+}-doped $GdVO_4$ powders. *Opt. Mater.* **35**, 1797–1804 (2013).
11. Yang, L., Li, L., Zhao, M., Fu, C. & Li, G. Is there lattice contraction in multicomponent metal oxides? Case study for $GdVO_4$:Eu^{3+} nanoparticles. *Nanotechnology* **24**, 305701(10pp) (2013).
12. Zheng, Y. *et al.* Facile hydrothermal synthesis and luminescent properties of large-scale $GdVO_4$:Eu^{3+} nanowires. *Cryst. Growth Des.* **9**, 5101–5107 (2009).

13. Xin, H., Lin, L. X., Wu, J. H. & Yan, B. Hydrothermal synthesis and multi-color photoluminescence of $GdVO_4$:Ln^{3+} (Ln = Sm, Dy, Er) sub-micrometer phosphors. *J. Mater. Sci. Mater. Electron.* **22**, 1330–1334 (2011).
14. Yin, W. *et al.* Lanthanide-doped $GdVO_4$ upconversion nanophosphors with tunable emissions and their applications for biomedical imaging. *J. Mater. Chem.* **22**, 6974–6981(2012).
15. Eastoe, J., Hollamby, M. J. & Hudson, L. Recent advances in nanoparticle synthesis with reversed micelles. *Adv. Colloid Interface Sci.* **128–130**, 5–15 (2006).
16. Malik, M. A., Wani, M. Y. & Hashim, M. A. Microemulsion method: a novel route to synthesize organic and inorganic nanomaterials. *Arab. J. Chem.* **5**, 397–417 (2012).
17. Tovstun, S. A. & Razumov, V. F. Preparation of nanoparticles in reverse microemulsions. *Russ. Chem. Rev.* **80**, 953–969 (2011).
18. Jovanović, D. J., Validžić, I. L. j., Janković, I. A., Bibić, N. & Nedeljković, J. M. Synthesis and characterization of shaped ZnS nanocrystals in water in oil microemulsions. *Mater. Lett.* **61**, 4396–4399 (2007).
19. Charinpanitkul, T., Chanagul, A., Dutt, J., Rungsardthong, U. & Tanthapanichakoon, W. Effects of cosurfactant on ZnS nanoparticle synthesis in microemulsion. *Sci. Technol. Adv. Mater.* **6**, 266–271 (2005).
20. Qi, L. in *Encyclopedia of Surface and Colloid Science*, Ch. Synthesis of inorganic nanostructures in reverse micelles, 6183–6207 (Taylor and Francis, London, UK, 2006)
21. Hall, D. G. *Nonionic Surfactants. Physical Chemistry* (ed. Schick, M. J.) (Marcel Dekker, New York, USA, 1987).
22. Nikolić, M. G., Jovanović, D. J. & Dramićanin, M. D. Temperature dependence of emission and lifetime in Eu^{3+}- and Dy^{3+}-doped $GdVO_4$. *Appl. Optics* **52**, 1716–1724 (2013).
23. Pileni, M. P. Reverse micelles used as templates: a new understanding in nanocrystal growth. *J. Exp. Nanosci.* **1**, 13–27 (2006).
24. Yang, L., Li, L., Zhao, M. & Li, G. Size-induced variations in bulk/surface structures and their impact on photoluminescence properties of $GdVO_4$:Eu^{3+} nanoparticles. *Phys. Chem. Chem. Phys.* **14**, 9956–9965 (2012).
25. Xu, W. *et al.* Controllable synthesis and size-dependent luminescent properties of YVO_4:Eu^{3+} nanospheres and microspheres. *J. Phys. Chem. C* **114**, 14018–14024 (2010).
26. Wang, G. *et al.* Enhanced photoluminescence of water soluble YVO_4:Ln^{3+} (Ln = Eu, Dy, Sm, and Ce) nanocrystals by Ba^{2+} doping. *J. Phys. Chem. C* **112**, 17042–17045 (2008).
27. Krumpel, A. H. *et al.* Lanthanide 4f-level location in AVO_4:Ln^{3+} (A = La, Gd, Lu) crystals. *J. Phys. Condens. Matter.* **21**, 115503(8pp) (2009).
28. Xu, Z. *et al.* Uniform and well-dispersed $GdVO_4$ hierarchical architectures: hydrothermal synthesis, morphology evolution, and luminescence properties. *Cryst. Eng. Comm.* **14**, 5530–5538 (2012).
29. Tanner, P. A. *Lanthanide Luminescence: Photophysical, Analytical and Biological Aspects, Lanthanide Luminescence in Solids* (eds: Hänninen, P. & Härmä, H.) (Springer series on fluorescence, Springer Verlag, Heidelberg, Germany, 2011).
30. Tanner, P. A., Yeung, Y. Y. & Ning, L. What factors affect the $^5D_0$ energy of Eu^{3+}? An investigation of nephelauxetic effects. *J. Phys. Chem. A* **117**, 2771–2781 (2013).
31. Chen, Z. *et al.* Effect of Li^+ ions doping on microstructure and upconversion emission of $Y_2Ti_2O_7$:Er^{3+}/Yb^{3+} nanophosphors synthesized via a sol-gel method. *J. Am. Ceram. Soc.* **96**, 1857–1862 (2013).
32. Sun, J., Xue, B. & Du, H. Synthesis and luminescence properties of Gd_6MoO_{12}:Yb^{3+}, Er^{3+} phosphor with enhanced photoluminescence by Li^+ doping. *Infrared Phys. Techn.* **60**, 10–14 (2013).
33. Liu, G. & Chen, X. in *Handbook on the Physics and Chemistry of Rare Earths Vol. 37*, (Eds: Gschneidner, K. A. Jr., Bünzli, J.-C. G. & Pecharsky, V. K.), Ch. 233 Spectroscopic Properties of Lanthanides in Nanomaterials, 99–169 (Elsevier B.V., London, UK, 2007).
34. Haase, M. & Schäfer, H. Upconverting nanoparticles. *Angew. Chem. Int. Ed.* **50**, 5808–5829 (2011).
35. Naruke, H., Mori, T. & Yamase, T. Luminescence properties and excitation process of a near-infrared to visible up-conversion color-tunable phosphor. *Opt. Mater.* **31**, 1483–1487 (2009).
36. Brites, C. D. S. *et al.* Thermometry at the nanoscale. *Nanoscale* **4**, 4799–4829 (2012).
37. Jaque, D. & Vetrone, F. Luminescence nanothermometry. *Nanoscale* **4**, 4301–4326 (2012).
38. Fischer, L. H., Harms, G. S. & Wolfbeis, O. S. Upconverting nanoparticles for nanoscale thermometry. *Angew. Chem. Int. Ed. Engl.* **50**, 4546–4551 (2011).
39. Debasu, M. L. *et al.* All-in-one optical heater-thermometer nanoplatform operative from 300 to 2000 K based on Er^{3+} emission and blackbody radiation. *Adv. Mater.* **25**, 4868–4874 (2013).
40. Vetrone, F. *et al.* Temperature sensing using fluorescent nanothermometers. *ACS Nano* **4**, 3254–3258 (2010).
41. Zhou, S. *et al.* Upconversion luminescence of $NaYF_4$:Yb^{3+},Er^{3+} for temperature sensing. *Opt. Commun.* **291**, 138–142 (2013).

Acknowledgments

Financial support for this study was granted by the Ministry of Education and Science of the Republic of Serbia (grant number 45020). The authors are grateful to P.S. Ahrenkiel for TEM measurements.

Author contributions

T.G. and D.J. conducted the nanoparticle synthesis. M.D., D.J. and T.G. contributed to the photoluminescence measurements. V.L. performed XRD measurements and structural analysis. D.J. and M.D. carried out data analysis. M.D. supervised research. D.J. and M.D. wrote the manuscript.

Additional information

Competing financial interests: The authors declare no competing financial interests.

How to cite this article: Gavrilović, T.V., Jovanović, D.J., Lojpur, V. & Dramićanin, M.D. Multifunctional Eu^{3+}- and Er^{3+}/Yb^{3+}-doped $GdVO_4$ nanoparticles synthesized by reverse micelle method. *Sci. Rep.* **4**, 4209; DOI:10.1038/srep04209 (2014).